The Effects of Pointing Error Sources on Energy Delivery from Orbiting Solar Reflectors

Moore, Iain; Sulbhewar, Litesh; Çelik, Onur; McInnes, Colin R.

DOI
10.1016/j.actaastro.2024.06.020

Publication date
2024

Document Version
Final published version

Published in
Acta Astronautica

Citation (APA)
Moore, I., Sulbhewar, L., Çelik, O., & McInnes, C. R. (2024). The Effects of Pointing Error Sources on Energy Delivery from Orbiting Solar Reflectors. *Acta Astronautica*, *222*, 563-572. https://doi.org/10.1016/j.actaastro.2024.06.020

Acta Astronautica 222 (2024) 563–572

Contents lists available at ScienceDirect

Acta Astronautica

journal homepage: www.elsevier.com/locate/actaastro

Research paper

The Effects of Pointing Error Sources on Energy Delivery from Orbiting Solar Reflectors[☆]

Iain Moore [*], Litesh Sulbhewar, Onur Çelik, Colin R. McInnes

James Watt School of Engineering, University of Glasgow, University Avenue, Glasgow, G12 8QQ, Scotland, UK

ARTICLE INFO

Keywords:
Orbiting solar reflectors
Sensor noise
PD control
Energy

ABSTRACT

Many proposals are being made for cleaner, more sustainable forms of energy production. Terrestrial solar photovoltaic farms (SPFs) could potentially deliver large quantities of energy to the grid, although these are limited to daytime use. The output from these SPFs could be enhanced, particularly around dawn and dusk, by the use of orbiting solar reflectors (OSRs) in near-polar orbit. These would reflect an image of the solar disk, or solar image (SI), onto the SPFs to augment their energy output. Pointing requirements are therefore to ensure that reflected sunlight is delivered to the terrestrial SPF, avoiding the losses incurred by an offset of the SI and the SPF itself. The SI would typically be of order 10 km for a reflector in a 1000 km orbit. Given the potentially large size of the reflectors, this presents a challenge for the attitude determination and control system (ADCS) to ensure that the maximum quantity of energy can be delivered to a SPF, typically requiring large control moment gyro actuators. In addition, there exist numerous sources of error in the ADCS which can cause further degradation in the quantity of energy delivered to the SPF. These errors can manifest in the resolution of the various sensors, flexible structural modes, manufacturing inaccuracies, and misalignments due to vibration during launch. This paper will investigate the effects of pointing error sources (PES) on the reflector ADCS and so on the quantity of energy delivered to the SPF. With the application of a PD controller with feedforward compensation, and the set of noise characteristics defined in this paper, numerical simulations will show the typical losses in energy delivered to SPFs of 0.015% when the model accounts for PES in onboard sensors, actuator uncertainty and flexible structural modes.

1. Introduction

The proposal for delivering energy from space has almost a century of history, beginning with the work of Oberth in 1929 [1]. Further advances in the concept came later in the 20th century when Enger presented a feasibility study of OSRs [2], which was followed by Ehricke [3] who detailed the potential uses of light reflected from space to the Earth, including an analysis of the energy that could be delivered to terrestrial SPFs. A NASA technical report [4] then followed with a comprehensive analysis of the use of OSRs for energy delivery to the Earth. More recently, Fraas et al. have produced a series of works on the subject [5–7] where constellations are proposed to deliver energy to SPFs both at night and during dawn/dusk hours. More recently, this work was continued with a feasibility study for the MiraSolar proposal [8]. The SOLSPACE project at the University of Glasgow provided a review of the literature on OSRs [9]. Additionally, the group has been developing OSR concepts and provided a reference architecture [10] which details a comprehensive study of orbits, control, structures and economic/regulatory considerations. A study was also conducted on actuator scaling laws for OSRs where it was found Control Moment Gyroscopes (CMG) were the preferred control actuator for these large structures [11]. More recently, work has investigated the enhancements to energy delivery made possible by a constellation of OSRs [12].

With OSRs purposed for delivering solar energy to SPFs [13–15], the objective is to deliver the maximum possible energy to the SPF. There are a number of factors, such as the reflectivity of the OSR and atmospheric losses, which will reduce the amount of energy which reaches the SPF. However, an additional factor, which does not appear to have been analysed for the OSR concept, is the effect of sensor noise and actuator uncertainties in the energy delivered to the SPF. Additionally, there has been a proposal for the use of displaced non-keplerian orbits for OSRs [16], where the pointing accuracy is again very important.

[☆] Content of this manuscript presented at the 74th International Astronautical Congress, Baku, Azerbaijan, 2-6 October 2023. Copyright by the authors. Paper number IAC-23,C1,1,6,x76505.

[*] Corresponding author.
E-mail address: iain.moore@glasgow.ac.uk (I. Moore).

https://doi.org/10.1016/j.actaastro.2024.06.020
Received 4 December 2023; Received in revised form 12 May 2024; Accepted 11 June 2024

The onboard sensors and actuators of a spacecraft can suffer from noise and uncertainties. Often, preliminary design simulations do not account for these uncertainties. However, their effects can be considerable. Additionally, the large structure required for the SOLSPACE project can exhibit significant flexible modes. This flexibility can result in additional torques which must be counteracted by the active control system.

As a related example, following the Cassini mission to Saturn, a study was made of the pointing stability performance of the mission [17]. In this work, the sources of jitter were identified as imperfections in the manufacture of the reaction wheels, low-g fuel sloshing, and sensor noise. Sensor noise with significant frequency content in the spacecraft bandwidth can appear as commands to the attitude controller. As the spacecraft responds to these commands, jitter results. Pelinski and Lee also identified structural vibrations as a source of jitter, and the residual structural vibrations after a slew manoeuvre can be considerable. It was also noted by the authors that the time at which the science phase begins after the slew manoeuvre is critical in jitter considerations. As the SOLSPACE project requires immediate use of the reflector at the end of a transitional slew manoeuvre from the idle phase to the tracking phase, this effect is required to be considered.

As a method to simulate sensor noise, Algrain and Powers [18] provide a tutorial-type discussion on methods for simulating star trackers, inertial measurement units (IMUs), gyroscopes, controllers and reaction wheels. Of particular interest to this work are the methods by which the star tracker, IMU and gyroscope noise are modelled. It is noted that the various noise sources on the gyroscope are simply a sum of the true value with the sources of noise.

A study was also conducted of the pointing stability for the James Webb Space Telescope (JWST) [19]. This work took an in-depth look at the required pointing for the JWST and consideration of the impact of noise on the pointing stability. The JWST would use the basic Chandra mission attitude determination and control system (ADCS) architecture. The actuation would be performed by reaction wheels, while gyroscopes and star trackers provided attitude determination. The JWST had an additional Fine Guidance Sensor (FGS), which utilised the telescope optics as an additional star tracker, able to attenuate much of the ADCS low frequency jitter.

The problem of pointing error engineering has been standardised in Europe, through the European Cooperation for Space Standardization (ECSS). At the behest of the European Space Agency (ESA), the ECSS produced the Pointing Error Engineering Handbook (ESSB-HB-E-003) [20]. This allowed for engineers to work to a common framework, implemented by the Pointing Error Engineering Tool (PEET) developed by Astos Solutions [21].

Following on from the reference architecture defined for the SOLSPACE project [10], this paper will investigate the effect of PES on the energy delivered to the Sun Cable SPF during an orbital pass. Section 2 will set out the different frames of reference used in this work and Section 3 will describe the orbital dynamics model used. Following this, the various PES will be described in Section 5. Then, Sections 6 and 7 will describe the rigid and flexible body dynamics respectively before the methods by which the structural modes are calculated are described in Section 8. The method by which the solar energy delivered is calculated is then described in Section 9 before the controller and estimation techniques are outlined in Section 10. At this point, the results of the simulation work will be presented in Section 11.

Part of this work was presented at the 74th International Astronautical Congress in Baku, Azerbaijan in October of 2023 with paper number IAC- 23,C1,1,6,x76505. Significant revisions were made for this publication.

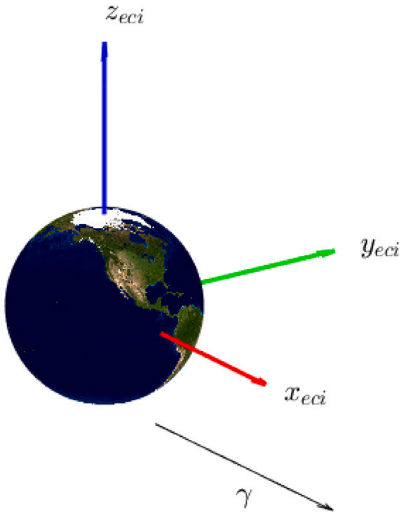

Fig. 1. Earth-centred inertial reference frame.

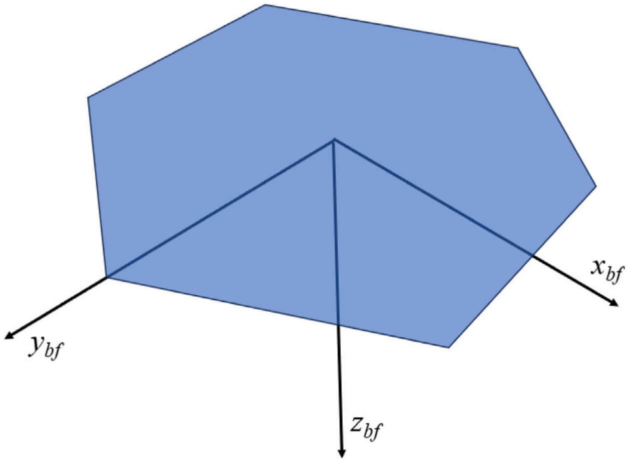

Fig. 2. Body-fixed reference frame.

2. Reference frames

Throughout this paper, a number of reference frames will be utilised. As such, this section will present those reference frames and the required rotation matrices for their transformations. The transformations from one reference frame to another was performed using the MATLAB™ Aerospace Toolkit, which contains a full library of the required conversions.

2.1. Earth-Centred Inertial

The Earth-Centred Inertial (eci) frame, shown in Fig. 1, has its origin at the centre of the Earth but does not rotate with the Earth. The x-axis points in the direction of the first point of Aries, while the z-axis points along the rotation axis of the Earth, with the positive direction towards the North pole. Finally, the y axis completes the right-handed set.

2.2. Body-fixed frame

All of the onboard sensors and actuators are referenced to the body-fixed (bf) reference frame, which is centred on the OSR centre-of-mass, with the x_{bf} and y_{bf} axes in the plane of the surface of the OSR and z_{bf} normal to the surface of the OSR, as shown in Fig. 2.

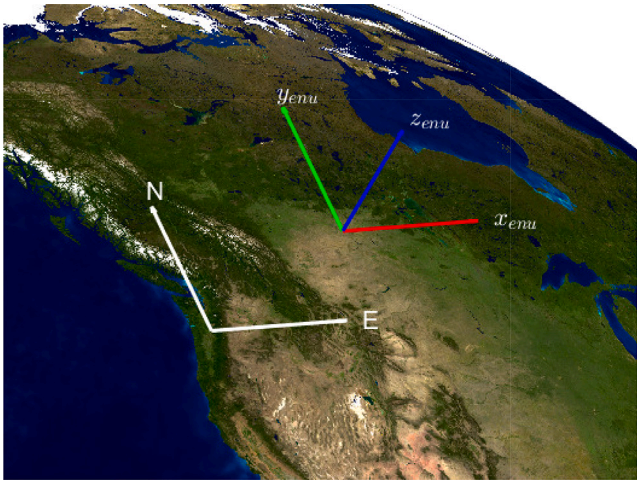

Fig. 3. Earth-North-Up reference frame.

Rotations between the bf and the Earth-centred inertial (eci) frames is achieved with the attitude matrix obtained via the attitude quaternion [22]:

$$\begin{aligned}
A(\mathbf{q})_{1,1} &= q_1^2 - q_2^2 - q_3^2 + q_4^2\\
A(\mathbf{q})_{2,2} &= -q_1^2 + q_2^2 - q_3^2 + q_4^2\\
A(\mathbf{q})_{3,3} &= -q_1^2 - q_2^2 + q_3^2 + q_4^2\\
A(\mathbf{q})_{1,2} &= 2(q_1 q_2 + q_3 q_4)\\
A(\mathbf{q})_{1,3} &= 2(q_1 q_3 - q_2 q_4)\\
A(\mathbf{q})_{2,3} &= 2(q_2 q_3 + q_1 q_4)
\end{aligned} \tag{1}$$

and so, the matrix is given by:

$$\mathbf{A}(\mathbf{q}) = \begin{bmatrix} A(\mathbf{q})_{1,1} & A(\mathbf{q})_{1,2} & A(\mathbf{q})_{1,3}\\ -A(\mathbf{q})_{1,2} & A(\mathbf{q})_{2,2} & A(\mathbf{q})_{2,3}\\ -A(\mathbf{q})_{1,3} & -A(\mathbf{q})_{2,3} & A(\mathbf{q})_{3,3} \end{bmatrix} \tag{2}$$

2.3. East-North-Up

For consideration of the solar image geometry on the Earth's surface, it is necessary to introduce a topocentric reference frame. In this case, the East-North-Up frame (enu) is used and shown in Fig. 3, where the frame is centred above a specified location on the Earth's surface, at a specified altitude, with the x axis pointing due-East, the y axis pointing North and the z-axis pointing normal to the x-y plane and radially outward from the Earth.

2.4. Azimuth-Elevation-Range

Further to the enu frame, a further topocentric frame is required in order to establish the geometry of the solar image (SI) which is reflected onto the Earth's surface by the OSR. This is the Azimuth-Elevation-Range (aer) frame. The elevation and range of the reflector relative to the SPF are required to establish the SI geometry, as will be detailed in Section 9. The azimuth angle is used to acquire the appropriate alignment of the SI ellipse major axis.

3. Orbital dynamics

The orbital dynamics model outlined in Ref. [23] is applied here, employing the J_2 perturbed Earth model:

$$\begin{aligned}
\ddot{x}_{eci} &= -\frac{\mu}{r_{eci}^3} x_{eci} + p_x\\
\ddot{y}_{eci} &= -\frac{\mu}{r_{eci}^3} y_{eci} + p_y\\
\ddot{z}_{eci} &= -\frac{\mu}{r_{eci}^3} z_{eci} + p_z
\end{aligned} \tag{3}$$

Table 1
Keplerian elements and initial condition of the reference architecture orbit.

Semi-major axis	7262.79 km
Eccentricity	0
Inclination	98.97°
Right ascension of ascending node	88°
$\theta_{gmst}(t_0)$	315°

where $[x_{eci}, y_{eci}, z_{eci}]^T$ are the Cartesian position coordinates in the eci frame, μ is the Earth's gravitational parameter, $r_{eci} = \sqrt{x_{eci}^2 + y_{eci}^2 + z_{eci}^2}$ and $\mathbf{p} = [p_x, p_y, p_z]^T$:

$$\mathbf{p} = -\frac{3}{2} J_2 \frac{\mu}{r_{eci}^2} \left(\frac{R_E}{r_{eci}}\right)^2 \begin{bmatrix} (1 - 5(\frac{z_{eci}}{r_{eci}})^2)(\frac{x_{eci}}{r_{eci}})\\ (1 - 5(\frac{z_{eci}}{r_{eci}})^2)(\frac{y_{eci}}{r_{eci}})\\ (3 - 5(\frac{z_{eci}}{r_{eci}})^2)(\frac{z_{eci}}{r_{eci}}) \end{bmatrix} \tag{4}$$

where R_E is the equatorial radius of the Earth and J_2 is the second order zonal harmonic coefficient which models the non-sphericity of the Earth.

The initial orbit has the Keplerian elements listed in Table 1.

4. SOLSPACE ADCS architecture

As detailed in Ref. [10], the SOLSPACE ADCS actuation is performed using a pyramid configuration of four Control Moment Gyros (CMGs), with a common skew angle of $\gamma_{sa} = 53.13°$. Attitude determination will be performed using the QUEST algorithm, utilising the star positions obtained from the star-tracker.

As this work required technical details to allow the modelling of noise, it is necessary to define which components are being used. In this respect, this paper attempts to utilise specifications similar to commercially available off-the-shelf (COTS) components. Otherwise, we aim to apply design values from other mission studies. The specifications chosen represent a conservative approach such that the results are not overly optimistic.

5. Pointing error sources

There are numerous potential sources of pointing error which can affect the pointing stability. In this paper, the sources which will be considered are noise in the star tracker (ST), gyroscope (GY), the gimbal angle and gimbal rates for the control moment gyros (CMGs), and static and dynamic imbalances in the CMG rotors. Additionally, the effects of a flexible body dynamic model (FLEX) are included.

5.1. Star-tracker

The principle attitude determination is performed using a star tracker. The geometry of a star tracker is the same as that of a pinhole camera [24]. If u-v represents the location on the image plane and f is the focal length. The unit vector from the spacecraft to a star is given by:

$$\hat{\mathbf{s}} = \frac{1}{\sqrt{f^2 + (u - u_0)^2 + (v - v_0)^2}} \begin{bmatrix} u - u_0\\ v - v_0\\ 1 \end{bmatrix} \tag{5}$$

where $[u_0, v_0]$ is the origin of the image plane. See Ref. [24] (figure 4.2) for a full description of the pinhole camera geometry. The elevation angles, α and β, can then be defined by $\alpha = \tan^{-1}(\hat{s}_x/\hat{s}_z)$ and $\beta = \tan^{-1}(\hat{s}_y/\hat{s}_z)$, and therefore:

$$\hat{\mathbf{s}} = \frac{1}{\sqrt{1 + \tan^2\alpha + \tan^2\beta}} \begin{bmatrix} \tan\alpha\\ \tan\beta\\ 1 \end{bmatrix} \tag{6}$$

Table 2
Star tracker parameters.

Stars in Catalog	12 443
Maximum Trackable Stars	15
Magnitude Limit	9
FOV	6° × 6°
σ_{st}	1.2 arc-sec

Table 3
Gyroscope parameters.

Angular Rate Walk	$0.019\ ''/\sqrt{s}$
Random Rate Walk	$0.00001\ ''/s^{3/2}$
Quantization	$0.02\ ''$
Bias	$0.001\ ''/s$

At this point, the Shuster noise model [25] is used to add noise to the elevation angles, where a small angles assumption leads to $\alpha = \hat{s}_x/\hat{s}_z$ and $\beta = \hat{s}_y/\hat{s}_z$. The covariance matrix for these parameters is then defined by:

$$\mathbf{R}_{cov} = \frac{\sigma^2}{1+\alpha^2+\beta^2}\begin{bmatrix}(1+\alpha^2)^2 & (\alpha\beta)^2 \\ (\alpha\beta)^2 & (1+\beta^2)^2\end{bmatrix} \tag{7}$$

The noise can then be obtained by:

$$\mathbf{z} = \mathbf{e}\begin{bmatrix}\lambda_1\phi \\ \lambda_2\phi\end{bmatrix} \tag{8}$$

where $\mathbf{e}$ is the matrix of eigenvectors of Eq. (7), λ_i $(i = 1,2)$ are the eigenvalues and ϕ is a zero-mean normally distributed random number. Therefore, the noisy elevation angles are obtained by:

$$\begin{bmatrix}\breve{\alpha} \\ \breve{\beta}\end{bmatrix} = \begin{bmatrix}\alpha \\ \beta\end{bmatrix} + \mathbf{z} \tag{9}$$

With this, the star location can be reconstructed using the noisy signals. Attitude determination is then performed using the QUEST algorithm described in Ref. [26]. The parameters for the star tracker are taken from a number of sources. The star catalog is obtained from Ref. [24], the maximum number of trackable stars is taken from Ref. [27], the magnitude limit is obtained as a best case from Ref. [28], the FOV is taken from Ref. [29] and the noise standard deviation, σ_{st}, is taken from Ref. [19]. These parameters are listed in Table 2.

5.2. Gyroscope

For the gyroscope, noise is added using normally distributed random numbers against the standard deviation value for each component of the sensor noise. The components of noise in the gyroscope are considered here to be the noise due to the angular rate walk ($\mathbf{z}_{arw}$), random rate walk ($\mathbf{z}_{rrw}$), quantisation noise ($\mathbf{z}_q$) and gyro bias ($\mathbf{z}_b$), the values of which are taken from a study of the ADCS requirements for the James Webb Space Telescope (JWST). The noisy signal is then obtained from:

$$\breve{\boldsymbol{\omega}} = \boldsymbol{\omega} + \mathbf{z}_{arw} + \mathbf{z}_{rrw} + \mathbf{z}_q + \mathbf{z}_b \tag{10}$$

where $\boldsymbol{\omega}$ is the true value of the spacecraft attitude angular velocity and $\breve{\boldsymbol{\omega}}$ is the noisy value. The noise parameters for the gyroscope are obtained from Ref. [19] and are given in Table 3.

5.3. Control Moment Gyro

The CMG uncertainties are modelled as additive white Gaussian noise (AWGN) on the gimbal angle and the gimbal rotational velocity. The values for the signal-to-noise ratio (SNR) for each of these was chosen from the Honeywell M-50 CMG datasheet and the values are listed in Table 4.

Table 4
CMG noise parameters.

Gimbal Angle SNR	100
Gimbal Rate SNR	100

Additionally, the static and dynamic imbalances of the CMG rotor are also simulated, and treated here as external torques on the system [24,30]. The static imbalance is the condition that the rotor centre-of-mass is not on the axis of rotation [24]. This results from manufacturing inaccuracies and produces a radial force from each CMG of [30]:

$$\mathbf{F}_{s,i} = U_{s,i}\omega_r^2\hat{\mathbf{u}}_i(t) \tag{11}$$

where subscript i refers to the ith CMG, U_s is the static imbalance parameter, ω_r is the angular velocity of the rotor and $\hat{\mathbf{u}}(t)$ is a time-dependent arbitrary unit vector normal to the rotor spin axis. The resulting torque is then obtained from:

$$\boldsymbol{\tau}_{s,i} = \mathbf{F}_{s,i} \times \mathbf{R}_{r,i} \tag{12}$$

where $\mathbf{R}_r$ is the position of the rotor centroid in the bf frame is obtained from structural analysis of the OSR central bus [10] and CMG placement on that central bus, and is given by:

$$\mathbf{R}_r = \begin{bmatrix}6.25 & 10.83 & 7.5 \\ -6.25 & 10.83 & 7.5 \\ -6.25 & -10.83 & 7.5 \\ 6.25 & -10.83 & 7.5\end{bmatrix} m \tag{13}$$

where each row provides the coordinate of the ith CMG, where $i = 1,2,3,4$.

The dynamic imbalance is the condition that the axis of rotation of the rotor is not a principal axis [24], which requires a torque [30]:

$$\boldsymbol{\tau}_d = U_d\omega_r^2\hat{\mathbf{v}}(t) \tag{14}$$

where U_d is the dynamic imbalance parameter and $\hat{\mathbf{v}}(t)$ is a time-dependent arbitrary unit vector normal to the rotor spin axis.

Obtaining the static and dynamic imbalance coefficients is dependent on the manufacture and installation of each individual rotor. To obtain values to use here, those of the Honeywell M-50 datasheet are scaled to the mass of the rotors in this paper, and have values of $U_s = 5.25$ g-cm and $U_d = 131.25$ g-cm^2.

6. Rigid-body attitude dynamics

The quaternion representation of the rigid body dynamics and kinematics are given, in the bf reference frame, by [24]:

$$\begin{aligned}\mathbf{J}_{rb}\dot{\boldsymbol{\omega}} + \boldsymbol{\omega} \times \mathbf{J}_{rb}\boldsymbol{\omega} &= \boldsymbol{\tau}_{cmg} + \boldsymbol{\tau}_{ext} \\ \dot{\mathbf{q}} &= \frac{1}{2}\boldsymbol{\Omega}\mathbf{q}\end{aligned} \tag{15}$$

where $\mathbf{J}_{rb}$ is the rigid-body inertia tensor, $\boldsymbol{\tau}_{cmg}$ is the torque provided by the CMGs, $\boldsymbol{\tau}_{ext}$ is the external torques on the reflector, in this case from gravity gradient, and:

$$\boldsymbol{\Omega} = \begin{bmatrix}0 & -\omega_x & -\omega_y & -\omega_z \\ \omega_x & 0 & \omega_z & -\omega_y \\ \omega_y & -\omega_z & 0 & \omega_x \\ \omega_z & \omega_y & -\omega_x & 0\end{bmatrix} \tag{16}$$

The required angular momentum rate for the commanded torques from the controller are obtained from [10]:

$$\dot{\mathbf{H}}_{cmg} = -\boldsymbol{\tau}_u - \boldsymbol{\omega} \times \mathbf{H}_{cmg} \tag{17}$$

where $\boldsymbol{\tau}_u$ is the commanded control torque. The relationship between the angular momentum rate and the gimbal rates is given by:

$$\dot{\mathbf{H}}_{cmg} = H_{cmg}\mathbf{A}\dot{\boldsymbol{\delta}} \tag{18}$$

and the matrix $\mathbf{A}_{cmg}$ is given by:

$$\mathbf{A}_{cmg} = \begin{bmatrix} c\gamma_{sa}c\delta_{g,1} & s\delta_{g,2} & c\gamma_{sa}c\delta_{g,3} & -s\delta_{g,4} \\ -s\delta_1 & -c\gamma_{sa}c\delta_{g,2} & s\delta_{g,3} & c\gamma_{sa}c\delta_{g,4} \\ s\gamma_{sa}c\delta_{g,1} & s\gamma_{sa}c\delta_{g,2} & s\gamma_{sa}c\delta_{g,3} & s\gamma_{sa}c\delta_{g,4} \end{bmatrix} \tag{19}$$

where c abbreviates the $\cos$ function and s abbreviates the $\sin$ function and $\boldsymbol{\delta}_g = [\delta_{g,1}, \delta_{g,2}, \delta_{g,3}, \delta_{g,4}]$ is a vector containing the gimbal angle for each of the four CMGs. The gimbal rates are then obtained from:

$$\dot{\boldsymbol{\delta}}_g = \frac{1}{H_{cmg}}\mathbf{A}^*_{cmg}\mathbf{H}_{cmg} \tag{20}$$

and the pseudoinverse is given by:

$$\mathbf{A}^*_{cmg} = \mathbf{A}^T_{cmg}(\mathbf{A}_{cmg}\mathbf{A}^T_{cmg})^{-1} \tag{21}$$

7. Flexible-body attitude dynamics

As the flexible modes for a large structure, such as the proposed reflector, can be considerable in magnitude, the coupled attitude/structural dynamics used for modelling of flexible structures are given, in the bf reference frame, by [31]:

$$\begin{aligned} \mathbf{J}_{rb}\dot{\boldsymbol{\omega}} + \boldsymbol{\delta}^T_f\ddot{\boldsymbol{\eta}} + \tilde{\boldsymbol{\omega}}(\mathbf{J}_{fb}\boldsymbol{\omega} + \boldsymbol{\delta}^T_f\dot{\boldsymbol{\eta}}) &= \boldsymbol{\tau}_{cmg} + \boldsymbol{\tau}_{ext} \\ \ddot{\boldsymbol{\eta}} + \mathbf{C}\dot{\boldsymbol{\eta}} + \mathbf{K}\boldsymbol{\eta} &= -\boldsymbol{\delta}_f\dot{\boldsymbol{\omega}} \end{aligned} \tag{22}$$

where the flexible-body inertia tensor $\mathbf{J}_{fb} = \mathbf{J}_{rb} + \boldsymbol{\delta}^T_f\boldsymbol{\delta}_f$, $\boldsymbol{\delta}_f$ is an $N \times 3$ matrix containing the coupling coefficients of the rotational and structural dynamics for the N flexible modes, obtained in Section 8, $\boldsymbol{\eta}$ is the array of modal coordinates, $\mathbf{C} = \mathrm{diag}(2\zeta_i\omega_{n,i}, i = 1, \ldots, N)$ is a matrix containing the damping for the N flexible modes, $\mathbf{K} = \mathrm{diag}(\omega^2_{n,i}, i = 1, \ldots, N)$, $\omega_{n,i}$ is the natural frequency of the ith mode, ζ_i is the damping of the ith mode and $\tilde{\boldsymbol{\omega}}$ is the cross product dyad given by:

$$\tilde{\boldsymbol{\omega}} = \begin{bmatrix} 0 & -\omega_3 & \omega_2 \\ \omega_3 & 0 & -\omega_1 \\ -\omega_2 & \omega_1 & 0 \end{bmatrix} \tag{23}$$

Rearranging Eqs. (22) for implementation gives:

$$\begin{aligned} \dot{\boldsymbol{\omega}} &= \mathbf{J}^{-1}_{rb}\left[-\tilde{\boldsymbol{\omega}}(\mathbf{J}_{fb}\boldsymbol{\omega} + \boldsymbol{\delta}^T_f\dot{\boldsymbol{\eta}}) + \boldsymbol{\delta}^T_f(\mathbf{K}\boldsymbol{\eta} + \mathbf{C}\dot{\boldsymbol{\eta}}) + \boldsymbol{\tau}_{cmg} + \boldsymbol{\tau}_{ext}\right] \\ \ddot{\boldsymbol{\eta}} &= -\boldsymbol{\delta}_f\dot{\boldsymbol{\omega}} - (\mathbf{K}\boldsymbol{\eta} + \mathbf{C}\dot{\boldsymbol{\eta}}) \end{aligned} \tag{24}$$

8. Structures

The structural configuration of the proposed reflector of SOLSPACE project is described in detail in Ref. [10]. The Finite Element model which accounts for all the mass elements present in the system is developed using ABAQUS®. The non-structural masses are simulated as distributed masses over the appropriate structural elements. The base of the structure is fixed as shown in Fig. 4. The total mass of the structure is 3051.5 kg with the inertia tensor, about the origin of the bf frame, given by:

$$\mathbf{J}_{rb} = \begin{bmatrix} 2.33 \times 10^7 & 5.00 & 0.00 \\ 5.00 & 2.32 \times 10^7 & 0.00 \\ 0.00 & 0.00 & 4.53 \times 10^7 \end{bmatrix} \text{kg m}^2 \tag{25}$$

The based fixed natural frequency analysis is carried out to obtain the modal parameters. The material damping of 0.002 is used for the composite material [32].

9. Solar image and energy delivery

In this paper, the SPF is assumed to be circular in shape with a diameter of 10 km. Given that the curvature of the Earth over 10 km is not significant, both the SPF and reflected solar image will be considered 2-dimensional on the x_{enu}-y_{enu} plane. As such, the SI will appear elliptical in shape which will reduce to a circle when directly overhead the SPF [13]. The surface of the OSR is considered to be perfectly flat throughout the work contained in this paper. The analysis which relates to a flexible structure will only consider the torques that this flexibility introduces to the system, and not on the effect on reflected light. The semi-minor and semi-major axes of the SI ellipse can be obtained from [13]:

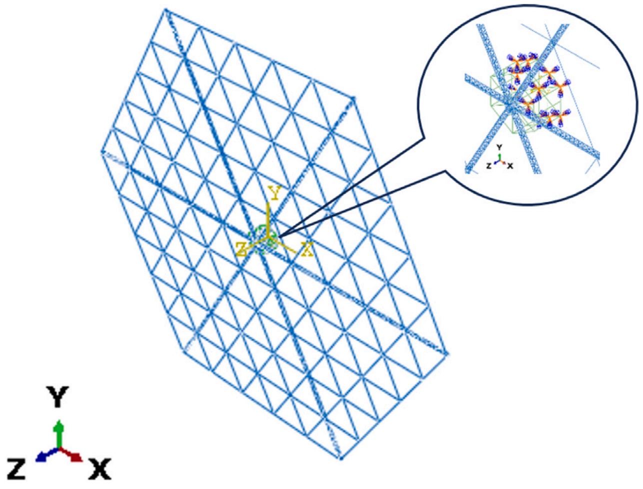

Fig. 4. OSR structure with base fixed boundary condition.

$$b = r_s \tan\frac{\nu}{2} \tag{26}$$

$$a = \frac{b}{\sin\epsilon} \tag{27}$$

where r_s is the magnitude of the slant range vector, ν is the angle subtended by the Sun, and has the value $\nu = 0.0093$ rad at 1 AU and ϵ is the elevation of the OSR with respect to the SPF, measured from local horizontal.

The area of the solar image on the ground can then be obtained by:

$$A_{im} = \pi ab \tag{28}$$

The area of the solar image directly influences the power density of the solar image on the ground by [13]:

$$\sigma_M = I_0\frac{A_r}{A_{im}(t)}\cos\frac{\psi}{2} \tag{29}$$

where I_0 is the solar constant, A_r is the area of the reflector and ψ is the angle between the incident light and reflected light vectors.

The power delivered to the solar farm can then be obtained from:

$$P_{sf} = \sigma_M A_{sf} \tag{30}$$

where A_{sf} is the fixed area of the solar farm. However, in order to understand the energy delivery, it is necessary to consider instead the time-varying effective area of the solar farm, $A_{sf}(t)$, which is the area where the solar image and the solar farm overlap, as shown in Fig. 5.

This process of calculating $A_{sf}(t)$ was previously approached in both an analytical [13,14] and numerical way [33]. However, in this paper, we fix a square grid which encloses the SPF. The length of each side of the square grid is 10% larger than the diameter of the circular SPF. The objective is then to use the binary mask technique from image processing to find which points lie both inside the circle of the SPF and the ellipse of the SI. To do this, the grid is discretised into small squares, or image pixels, of equal size. The side length of each square, which can also be considered the resolution of the image, is chosen as 100 m, as this gave the best balance between performance, in terms of computation time, and accuracy of the calculated area. Initially, the entire binary mask is set as zero. Then, only those points which lie inside both the SPF and the SI are given the value 1. It is then simply a case of summing the area for each pixel for which the binary mask has value 1.

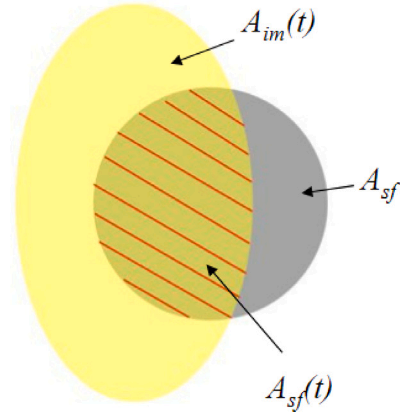

Fig. 5. Solar Image Geometry, where $A_{im}(t)$ is the time-varying area of the SI ellipse, A_{sf} is the fixed SPF area and $A_{sf}(t)$ is the time-varying area where the SI and SPF converge.

It is also necessary to account for losses due the imperfect reflection of the reflector as well as due to the Earth's atmosphere. In this work, the reflectivity coefficient is set as $\xi_r = 0.92$ and the atmospheric losses are given by [13]:

$$\xi_a = 0.1283 + 0.7559 e^{-0.3878 \sec(\frac{\pi}{2} - \epsilon)} \tag{31}$$

and so the power after losses is given by:

$$P_{sf}(t) = \xi_r \xi_a \sigma_M A_{sf}(t) \tag{32}$$

This paper will establish the losses in power delivered to the SPF due to various PES. As such, a new coefficient is established which is the averaged power delivery factor, $\bar{\xi}_p$. This then leads to:

$$P_{sf}(t) = \bar{\xi}_p \xi_r \xi_a \sigma_M A_{sf}(t) \tag{33}$$

The energy delivered is then obtained by integrating the power over the time of the pass:

$$E = \int_0^{T_{Pass}} P_{sf}(t) dt \tag{34}$$

where T_{Pass} is the time at the end of the pass, where the OSR passes below the local horizon.

10. Control and estimation design

10.1. Proportional-derivative control

The controller applied in this paper follows that of Ref. [10], where the control torque is calculated using PD control logic with feedforward compensation:

$$\boldsymbol{\tau}_u = -\mathbf{K}_p \mathbf{q}_e - \mathbf{K}_d \boldsymbol{\omega}_e + \boldsymbol{\omega} \times \mathbf{J}_{rb} \boldsymbol{\omega} + \mathbf{J}_{rb} \dot{\boldsymbol{\omega}}_t \tag{35}$$

where $\boldsymbol{\omega}_t$ is the angular velocity of the SPF, $\boldsymbol{\omega}_e = \boldsymbol{\omega} - \boldsymbol{\omega}_t$, $\mathbf{K}_p - 2k\mathbf{J}_{rb}$ is the proportional gain matrix with $k = \omega_b^2 + (2\zeta\omega_b)/T$, and $\mathbf{K}_d = c\mathbf{J}_{rb}$ is the derivative gain matrix with $c = 2\zeta\omega_b + 1/T$, and $\mathbf{q}_e$ is the error quaternion, given by:

$$\mathbf{q}_e = \bar{\mathbf{q}}_t \otimes \mathbf{q} \tag{36}$$

where $\bar{\mathbf{q}}_t$ is the conjugate of the target, or reference, quaternion for the desired pointing, which in the tracking phase is the quaternion which allows reflected light to reach the SPF. In this work, as with Ref. [10], the controller bandwidth, $\omega_b = 3$, damping ratio, $\zeta = 0.9$ and time constant,$T = 10$ s.

Table 5
Orbit and attitude initial conditions.

$\mathbf{r}_{0,eci}$	$[-1034.50, 1828.20, 6952.39]^T$ km
$\mathbf{v}_{0,eci}$	$[0.54, 7.16, 1.81]^T$ km/s
$\mathbf{q}_0$	$[0.50, 0.50, 0.50, 0.50]^T$
$\boldsymbol{\omega}_{0,bf}$	$[0.00, 0.00, 0.00]^T$ rad/s

10.2. The Quaternion Estimator

The Quaternion Estimator (QUEST) algorithm [26] is used here to estimate the spacecraft attitude from the noisy ST data, as obtained from the method presented in Section 5.

The objective of the QUEST algorithm is to find an orthogonal matrix A_{opt} which minimises the loss function:

$$L(A) = \frac{1}{2} \sum_{i=1}^{n_q} a_i |\bar{\boldsymbol{W}}_i - A\bar{\boldsymbol{V}}_i|^2 \tag{37}$$

where $a_i (i = 1, \ldots, n_q)$ are a set of non-negative weights, $\bar{\boldsymbol{W}}$ are the observed star positions and $\bar{\boldsymbol{V}}$ are the reference star positions. The gain function is then defined as:

$$g(A) = a_i \bar{\boldsymbol{W}}_i^T A \bar{\boldsymbol{V}}_i \tag{38}$$

$L(A)$ will be minimum where $g(A)$ is maximum, and so the objective is to find A_{opt} which maximises $g(A)$. This work will implement the QUEST function developed by Lourakis in Ref. [34]. Full details of the algorithm can be found in Refs. [26,35].

11. Results

The example SPF for this paper is set at the proposed Sun Cable location in Australia, which is proposed to be situated at −17.29° N, 133.50° E. In an effort to relate the work contained here to the work of Çelik and McInnes [13], the SPF is considered to be circular in shape and of 10 km in diameter.

11.1. Pointing error terminology

There are two pointing error terms used in this work, and set out by the European Cooperation on Space Standardization (ECSS). These are the Pointing Error Source(PES), Absolute Performance Error (APE) and the Relative Performance Error (RPE). APE gives the angular difference between the desired attitude and the actual attitude, and the RPE gives the difference between the APE at a specific point in time and the mean value of APE over a defined window of time, during which that instantaneous APE has been measured, and is defined by [20]:

$$e_{RPE}(t, \Delta t) = e_{APE}(t) - \bar{e}_{APE}(t, \Delta t) \tag{39}$$

where $\bar{e}_{APE}(t, \Delta t)$ is the mean value of the instantaneous error $e_{APE}(t)$ over a defined window of time. In this work, the window time for all simulations is 10 s.

11.2. Numerical simulation parameters

The dynamical equations contained in Eqs. (15) and (22) are integrated here using a fixed-step 4th order Runge Kutta integration, with step size of $\Delta t = 0.1$ s. A fixed-step integrator was chosen as, when using variable-step methods, the step size is prone to become very small in the presence of noise and the integration times become unmanageable.

Additionally, the orbit and attitude initial conditions are set as given in Table 5, where $\mathbf{r}_0$ and $\mathbf{v}_0$ are the initial position and velocity respectively, given in the eci reference frame, $\mathbf{q}_0$ is the initial attitude quaternion, which gives the OSR facing the Sun and is the initial condition imposed in Ref. [10] of which this work follows on, and $\boldsymbol{\omega}_0$ is the initial angular velocity of the OSR given in the bf frame.

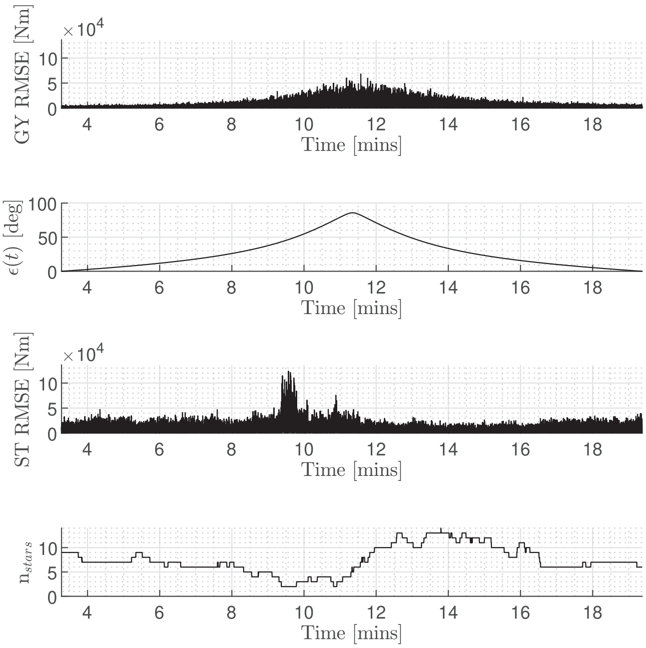

Fig. 6. Torque due to noise in star-tracker and gyroscope.

For simulation of the flexible-body system, the initial modal coordinates, $\boldsymbol{\eta}_0$, and modal coordinate velocities, $\dot{\boldsymbol{\eta}}_0$, are all set to zero.

As the values of pointing error in degrees can be very small, the arc-second unit is introduced, where 1 arc-hour = 1°. The arc-second is denoted by the symbol (") and so, 1" = $\frac{1}{3600}{}^{\circ}$.

11.3. Torque generated due to noise in each PES

In order to establish the torque which is generated by the noise/uncertainties around each sensor/actuator or dynamical model, the root mean square error (RMSE) is used. The RMSE is defined by:

$$RMSE = \sqrt{\frac{1}{n_s}\sum_{i=1}^{n_s} |A_i - F_i|} \tag{40}$$

where n_s is the number of sample points, A_i is the actual value at the ith sample point and F_i is the expected value at the ith sample point.

At each time point along the OSR trajectory, the RMSE of the $[x, y, z]_{bf}$ components of the torque for the noisy signal to the clean signal is obtained. Fig. 6 shows the RMSE for the gyroscope (GY) and the star-tracker (ST) along with the number of stars visible to the ST.

For the GY, the torque due to noise is found to follow the track of the elevation, $\epsilon(t)$. This means that the highest torque due to noise occurs at the zenith point, where the angular rates of the OSR during tracking are highest.

It is clear that the attitude estimation produced by the QUEST algorithm is dependent on the number of stars visible (n_{stars}). In fact, attitude estimation in the cross-boresight is known to be improved for increasing n_{stars} by a factor of $1/\sqrt{n_{stars}}$ [29]. The highest RMSE for the ST occurs at the points where n_{stars} is lowest. In contrast, a larger n_{stars} gives a better attitude estimation, and so the RMSE of torque due to ST noise is lowest at these points.

Following this, Fig. 7 shows the RMSE of torques produced due to noise in the control moment gyro (CMG) and from the flexible body dynamics (FLEX). The torque produced due to noise is largely constant for the CMGs, and the FLEX RMSE trend follows $\epsilon(t)$, with the maximum effect of this PES coming at the point of maximum $\epsilon(t)$. However, the magnitude of the FLEX RMSE shows that the effect of this PES is comparatively small.

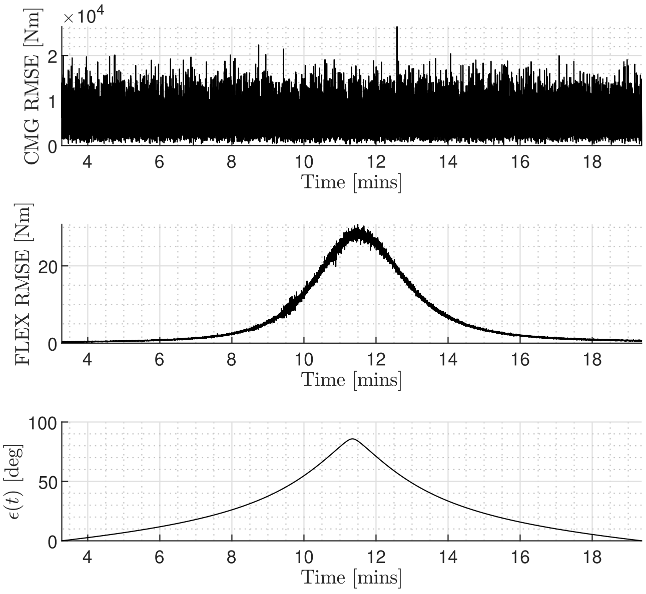

Fig. 7. Torque due to noise in control moment gyro and flexible body.

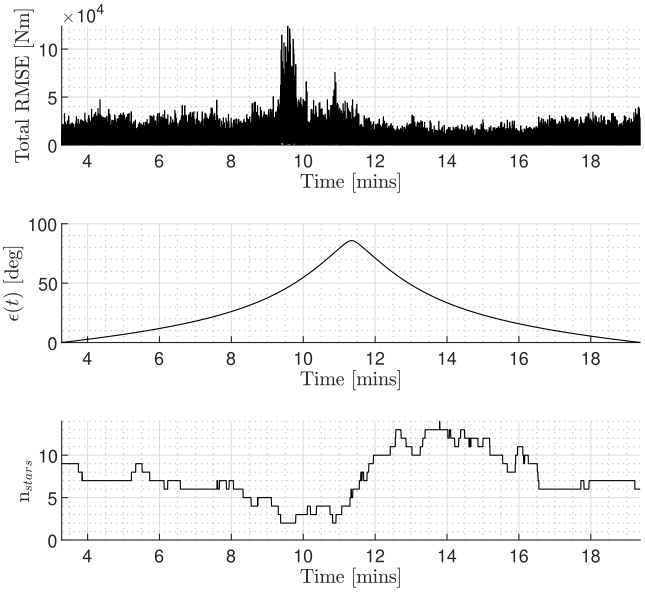

Fig. 8. Total torque due to sensor/actuator noise and flexible body dynamics.

Finally, the RMSE of the total torque of the clean system compared with the noisy system is shown in Fig. 8 along with $\epsilon(t)$ and n_{stars}. What is immediately noticeable is the profile of this noise generated torque is similar to the profile of the ST RMSE of Fig. 6. This shows that the ST dominates in terms of the torques generated due to noise in that PES.

11.4. Absolute and relative pointing errors

The APE for each PES in isolation is simulated to understand the magnitude of the pointing error related to that PES. Fig. 9 shows the APE resulting from noise in the CMGs remains largely constant throughout the pass over the Sun Cable SPF. The APE for the GY is also largely constant though with a small magnitude increase due to the GY drift. The magnitude of the APE for the ST is similar to that of the CMG, though with maximum values higher, showing that this is the dominant PES in the proposed system. Finally, the APE for the FLEX

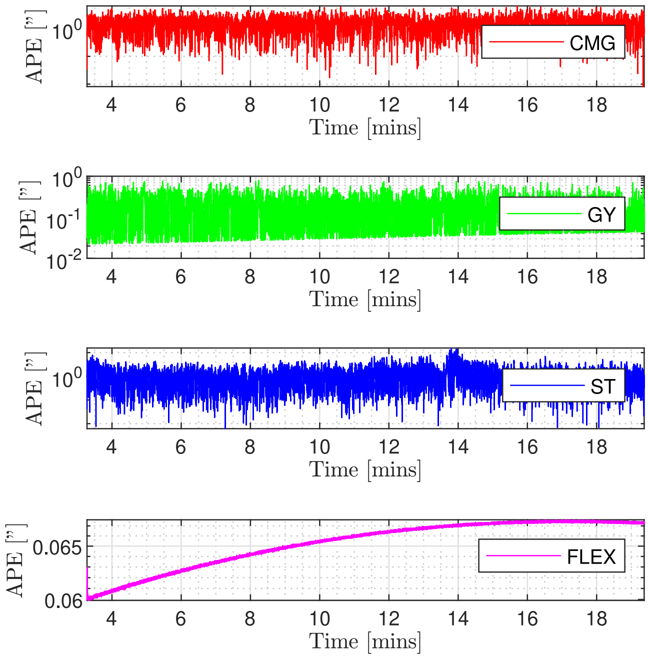

Fig. 9. APE for each PES simulated in isolation.

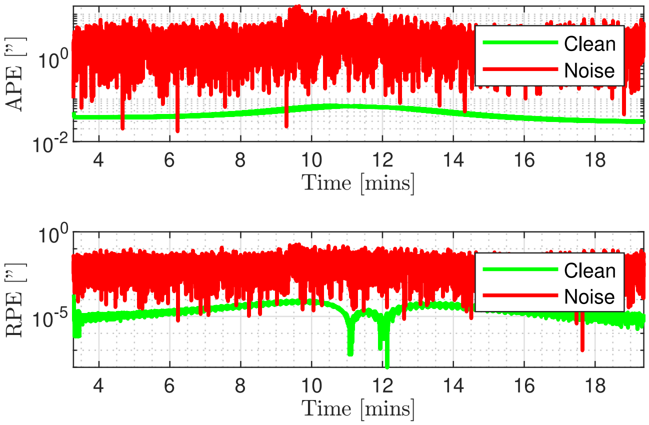

Fig. 10. APE and RPE for cumulative PES.

PES shows what appears to be a partially captured periodic behaviour. As the pass time at Sun Cable is approximately 17 min, the full periodic behaviour is not captured.

Having looked at each PES in isolation, the cumulative APE and RPE are shown in Fig. 10. For the noisy system, there is a small increase in both APE and RPE between 9 and 10 min. This coincides with the poorer attitude estimation from the ST due to a low number of visible stars, which was shown in Fig. 6. The cumulative effect of each PES is shown to produce a several orders magnitude increase in RPE and one to two orders magnitude increase in APE. However, both APE and RPE remain well within the tolerances to maintain the SI within the boundary of the SPF at high $\epsilon(t)$.

11.5. Solar energy delivery losses

The objective of this work is to show the effect on delivered energy from the OSR to the SPF when various PES are implemented in the system resulting in the increased APE and RPE shown in Fig. 10.

Fig. 11 shows the energy accumulation over time, the instantaneous power being delivered and the power loss factor, ξ_p, which is defined in Section 9. Due to the relatively small APE, the energy delivery is not largely affected. In fact, the loss in total energy delivered is only 0.015% for the noisy system as compared with the clean system.

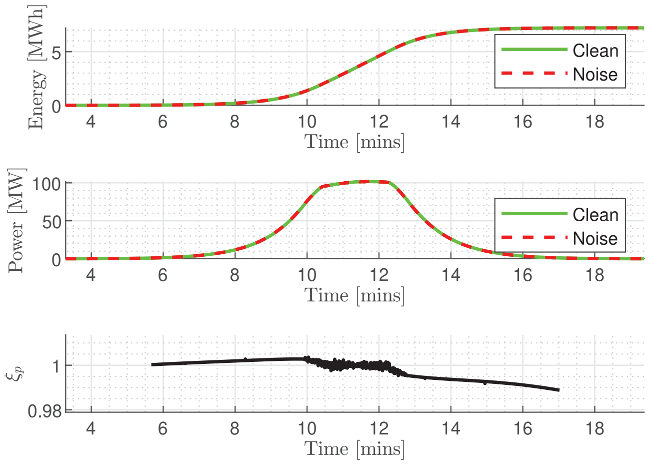

Fig. 11. Energy and power delivery to SPF.

Upon inspection of the ξ_p plot in Fig. 11, as the OSR approaches higher $\epsilon(t)$ relative to the SPF, there is a small increase in delivered power for the noisy system compared with the clean system. On this approach to zenith, Fig. 12 shows that the total reflected image area, $A_{im}(t)$, of the noisy system is smaller than that of the clean system. This is shown by the difference, defined by:

$$\Delta A_{im}(t) = A_{im,n}(t) - A_{im,c}(t) \tag{41}$$

where $A_{im,n}(t)$ is the SI image area for the noisy system and $A_{im,c}(t)$ is the SI image area for the clean system. This difference is due to the jitter in the noisy system varying the dimensions of the SI ellipse. For $A_{im,n}(t) < A_{im,c}(t)$, the power density, σ_M, is higher for the noisy system, resulting in a net power gain during this period for the noisy system, as shown by the positive $\Delta\sigma_M$ in Fig. 12, where:

$$\Delta\sigma_M(t) = \Delta\sigma_{M,n}(t) - \Delta\sigma_{M,c}(t) \tag{42}$$

Once the SI image boundary crosses the SPF boundary, there are also differences in the effective SPF area:

$$\Delta A_{sf}(t) = A_{sf,n}(t) - A_{sf,c}(t) \tag{43}$$

After the zenith point is passed, the value of ξ_p reduces such that power losses are experienced at the SPF. Overall, more power is lost than gained during the pass, resulting in a lower value of delivered energy for the noisy system.

For future work, a value of ξ_p which can be applied to account for losses due to the cumulative effect of numerous PES on the system is sought. For this, the mean value, $\bar{\xi}_p$, is taken and is $\bar{\xi}_p = 0.9978$

12. Conclusions

This paper has addressed the real-world problem of an imperfect pointing system onboard Orbiting Solar Reflectors (OSRs). It has been shown that the noise in the system leads to jitter as well as an increased absolute performance error (APE). When all sources of pointing error (PES) are considered, there is a 0.015% loss in energy delivered to the solar photovoltaic farm (SPF). When looking at the contribution from individual components, noise in the star-tracker and control moment gyroscopes contribute most to pointing errors and energy delivery losses. A power loss factor of $\bar{\xi}_p = 0.9978$ will be carried forward to future work to account for losses due to noise in the system.

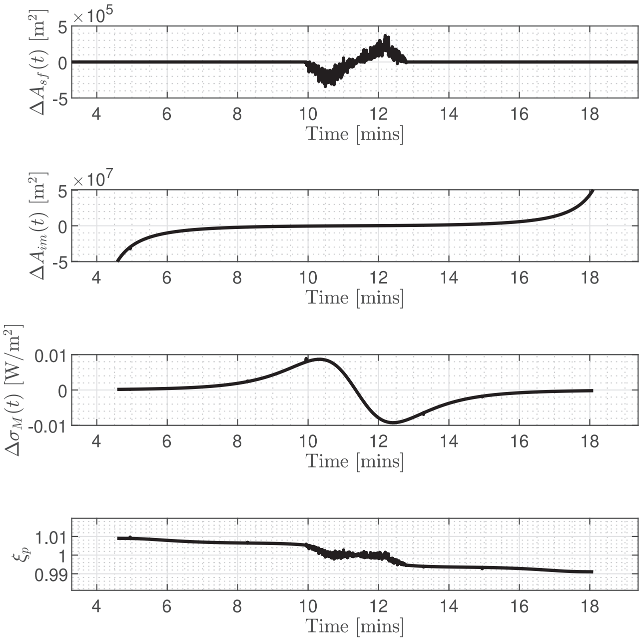

Fig. 12. Components of power delivery over time.

CRediT authorship contribution statement

Iain Moore: Formal analysis, Investigation, Methodology, Software, Validation, Visualization, Writing – original draft, Writing – review & editing. **Litesh Sulbhewar:** Formal analysis, Methodology, Software, Writing – original draft. **Onur Çelik:** Formal analysis, Methodology, Software. **Colin R. McInnes:** Funding acquisition, Project administration, Supervision.

Declaration of competing interest

The authors declare that they have no known competing financial interests or personal relationships that could have appeared to influence the work reported in this paper.

Acknowledgements

This project has received funding from the European Research Council (ERC) under the European Union's Horizon 2020 research and innovation programme (grant agreement No. 883730). CRM is also supported by the Department of Science, Innovation and Technology (DSIT) and the Royal Academy of Engineering, UK under the Chair in Emerging Technologies programme. For the purpose of open access, the author(s) has applied a Creative Commons Attribution (CC BY) licence to any Author Accepted Manuscript version arising from this submission.

Content of this manuscript was presented at the 74th International Astronautical Congress, Baku, Azerbaijan, 2-6 October 2023. Copyright by the authors. Paper number IAC-23,C1,1,6,x76505.

The authors would also like to thank the reviewers for their excellent comments and suggestions.

References

[1] H. Oberth, Ways to Spaceflight, third ed., 1929.

[2] R.C. Enger, Solar Electric Generating System Resource Requirements And The Feasibility Of Orbiting Solar Reflectors (Ph.D. thesis), US Air Force Institute of Technology, 1977.

[3] K.A. Ehricke, Space light: space industrial enhancement of the solar option, Acta Astronaut. 6 (12) (1979) 1515–1633, http://dx.doi.org/10.1016/0094-5765(79)90003-1.

[4] J.E. Canady, J.L. Allen, Illumination from space with orbiting solar-reflector spacecraft, Technical Report, NASA, NASA-TP-2065, 1982.

[5] L.M. Fraas, Mirrors in space for low-cost terrestrial solar electric power at night, in: 2012 38th IEEE Photovoltaic Specialists Conference, IEEE, 2012, pp. 002862–002867, http://dx.doi.org/10.1109/PVSC.2012.6318186.

[6] L.M. Fraas, G.A. Landis, A. Palisoc, Mirror satellites in polar orbit beaming sunlight to terrestrial solar fields at dawn and dusk, in: 2013 IEEE 39th Photovoltaic Specialists Conference, PVSC, IEEE, 2013, pp. 2764–2769, http://dx.doi.org/10.1109/PVSC.2013.6745046.

[7] L. Fraas, A. Palisoc, B. Derbes, Mirrors in dawn dusk orbit for low-cost terrestrial solar electric power in the evening, in: 51st AIAA Aerospace Sciences Meeting Including the New Horizons Forum and Aerospace Exposition, American Institute of Aeronautics and Astronautics, Reston, Virigina, 2013, http://dx.doi.org/10.2514/6.2013-1191.

[8] L.M. Fraas, M.J. O'Neill, Sunbeams from space mirrors for terrestrial PV, in: Low-Cost Solar Electric Power, Springer International Publishing, Cham, 2023, pp. 163–176, http://dx.doi.org/10.1007/978-3-031-30812-3_12.

[9] O. Çelik, A. Viale, T. Oderinwale, L. Sulbhewar, C.R. McInnes, Enhancing terrestrial solar power using orbiting solar reflectors, Acta Astronaut. 195 (2022) 276–286, http://dx.doi.org/10.1016/J.ACTAASTRO.2022.03.015.

[10] A. Viale, O. Çelik, T. Oderinwale, L. Sulbhewar, C.R. McInnes, A reference architecture for orbiting solar reflectors to enhance terrestrial solar power plant output, Adv. Space Res. 72 (4) (2023) 1304–1348, http://dx.doi.org/10.1016/j.asr.2023.05.037.

[11] A. Viale, C.R. McInnes, Attitude control actuator scaling laws for orbiting solar reflectors, Adv. Space Res. 71 (1) (2023) 604–623, http://dx.doi.org/10.1016/J.ASR.2022.10.015.

[12] O. Çelik, C.R. McInnes, A constellation design for orbiting solar reflectors to enhance terrestrial solar energy, Acta Astronaut. 217 (2024) 145–161, http://dx.doi.org/10.1016/j.actaastro.2024.01.031.

[13] O. Çelik, C.R. McInnes, An analytical model for solar energy reflected from space with selected applications, Adv. Space Res. 69 (1) (2022) 647–663, http://dx.doi.org/10.1016/j.asr.2021.10.033.

[14] O. Çelik, C.R. McInnes, A generic three-dimensional model for solar energy reflected from mirrors in circular orbits, Adv. Space Res. 72 (11) (2023) 5047–5069, http://dx.doi.org/10.1016/j.asr.2023.09.046.

[15] O. Çelik, C.R. McInnes, A constellation design for orbiting solar reflectors to enhance terrestrial solar energy, in: 74th International Astronautical Congress, Baku, Azerbaijan, 2023.

[16] O. Çelik, C.R. McInnes, Families of Displaced non-Keplerian Polar Orbits for Space-Based Solar Energy Applications, in: 73rd International Astronautical Congress, Paris, 2022.

[17] E.B. Pilinski, A.Y. Lee, Pointing-Stability Performance of the Cassini Spacecraft, J. Spacecr. Rockets 46 (5) (2009) 1007–1015, http://dx.doi.org/10.2514/1.41675.

[18] M.C. Algrain, R.M. Powers, Line-of-sight pointing accuracy/stability analysis and computer simulation for small spacecraft, in: M.K. Masten, L.A. Stockum (Eds.), Aerospace/Defense Sensing and Controls, 1996, pp. 62–76, http://dx.doi.org/10.1117/12.241943.

[19] L. Meza, F. Tung, S. Anandakrishnan, V. Spector, T. Hyde, Line of sight stabalization of james webb space telescope, in: 27th Annual AAS Guidance and Control Conference, Breckenridge, CO, 2005.

[20] ESSB-HB-E-003 Working Group, ESA pointing error engineering handbook, Technical Report, ESA, 2011.

[21] M. Casasco, S. Salehi, S. Weikert, J. Eggert, M. Hirth, H. Su, T. Ott, Pointing error engineering framework for high pointing accuracy missions, in: 24th International Symposium on Space Flight Dynamics, Laurel, MD (USA), 2014.

[22] J.R. Wertz, Spacecraft Attitude Determination and Control, Seventh ed., Kluwer Academic Publishers, London, 1990.

[23] H. Schaub, J.L. Junkins, Analytical Mechanics of Space Systems, fourth ed., AIAA, Reston, VA, 2018.

[24] F.L. Markley, J.L. Crassidis, Fundamentals of Spacecraft Attitude Determination and Control, Springer New York, New York, NY, 2014, http://dx.doi.org/10.1007/978-1-4939-0802-8.

[25] M.D. Shuster, Kalman filtering of spacecraft attitude and the QUEST model, J. Astronaut. Sci. 38 (3) (1990) 377–393.

[26] M.D. Shuster, S.D. Oh, Three-axis attitude determination from vector observations, J. Guid. Control 4 (1) (1981) 70–77, http://dx.doi.org/10.2514/3.19717.

[27] F. Leonardo, Leonardo finmeccanica AA-STR data sheet, 2017, URL https://electronics.leonardo.com/en/products/aastr.

[28] X. Zheng, Y. Huang, X. Mao, F. He, Z. Ye, Research status and key technologies of all-day star sensor, J. Phys. Conf. Ser. 1510 (1) (2020) 012027, http://dx.doi.org/10.1088/1742-6596/1510/1/012027.

[29] A.J. Swank, SWIR Star Tracking, Technical Report,, NASA/TM-20220007061, 2022.

[30] J. Alcorn, C.J. Allard, H. Schaub, Fully-Coupled Dynamical Jitter Modeling of a Rigid Spacecraft with Imbalanced Reaction Wheels, in: AIAA/AAS Astrodynamics Specialist Conference, American Institute of Aeronautics and Astronautics, Reston, Virginia, 2016, http://dx.doi.org/10.2514/6.2016-5686.

[31] S. Di Gennaro, Output stabilization of flexible spacecraft with active vibration suppression, IEEE Trans. Aerosp. Electron. Syst. 39 (3) (2003) 747–759, http://dx.doi.org/10.1109/TAES.2003.1238733.

[32] ECSS Secretariat, Structural materials handbook - Part 1: Overview and material properties and applications (ECSS-E-HB-32-20 Part 1A), Technical Report, Requirements and Standards Division, European Space Agency, 2011.

[33] A. Viale, O. Celik, T. Oderinwale, L. Sulbhewar, G. Bailet, C.R. McInnes, Towards the commercial development of orbiting reflectors: a technology demonstration roadmap, in: 73rd International Astronautical Congress, IAC–22–C3.2.X70070, Paris, 2022.

[34] M. Lourakis, Absolute orientation with the QUEST algorithm, 2017, http://www.mathworks.com/matlabcentral/fileexchange/65173.

[35] F.L. Markley, D. Mortari, Quaternion Attitude Estimation Using Vector Observations, J. Astronaut. Sci. 48 (2–3) (2000) 359–380, http://dx.doi.org/10.1007/BF03546284.